Results in Engineering 21 (2024) 101682

Contents lists available at ScienceDirect

Results in Engineering

journal homepage: www.sciencedirect.com/journal/results-in-engineering

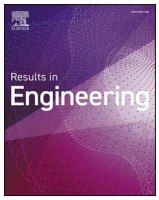

Analysis of super Cr13 stainless-steel internal fracture growth effects during skew mill piercing process

Hamed Aghajani Derazkola *, Eduardo García Gil, Alberto Murillo-Marrodan

Department of Mechanics, Design and Industrial Management, University of Deusto, 48007 Bilbao, Spain

ARTICLE INFO

Keywords:
Skew mill piercing
Super Cr13 stainless-steel
Fracture growth
FEM

ABSTRACT

The seamless tube piercing process of super Cr13 martensitic stainless steel is addressed in this paper by comparing industrial piercing tests, laboratory hot tensile tests for material behavior characterization, and finite element simulations. Particular focus is given to the effect of process parameters on internal fracture growth and geometrical homogeneity of the tube. The geometrical non-homogeneities found on industrial pierced tubes are closely related to the change of flow stress of super Cr13 stainless steel during the piercing process. This way, the non-uniform strain rate along the tube's cross-section during piercing affects the fracture growth and, consequently, the thickness homogeneity of the tube, which varies from tip to tail. Due to obtained results, the mean value of pierced tube perimeter is 660 mm, while the mean value of the tube perimeter in the FEM simulation was predicted to be 2 % more (675 mm). The contact temperature of the plug and piercing tube was predicted at 1100 °C, and the mean value of pierced tube diameter in the simulation (210 mm) was 1.5 % more than the mean value of the actual tube (207 mm). The morphology of δ-ferrite affects the origin of primary crack initiation during the piercing process. Short and thick grains of δ-ferrite created at low strain rates that lengthen with increasing strain rate affect fracture sensitivity at the tip of the plug, favoring the non-homogeneity of the material.

1. Introduction

Seamless tube manufacturing is a complex hot deformation process that transfers a billet to a tube at a high strain rate [1]. The main tools in this process are rollers, Diescher disks, and a plug. Several rollers and Diescher disks can be changed depending on the target tube. In some cases, the two rollers are used with two Diescher disks; in others, three rollers are used without Diescher disks. The rollers rotate during the process, and they are the main parts for deformation and moving forward of the billet during piercing [2]. Diescher disks are also rotating, controlling the tube's geometry to avoid over deformation of the tube [3]. The plug aims to pierce the tube internally and make a hole inside the billet. The plug is usually fixed without linear movements in X, Y, and Z directions; in some cases, it can be rotated on longitudinal axis. The material behavior during hot forming determines the tube quality and speed of manufacturing [4]. In some cases, the internal hole is produced by hot cracks, which is called the Mannesmann effect, and in some cases, the internal hole is produced by deformation. In the seamless tube piercing process, a notable challenge arises in the form of material sticking to the plug, particularly at the toe of the plug [5]. The toe of the plug refers to the leading edge that initiates the piercing of the tube. This issue can impede the smooth progress of the piercing operation, leading to disruptions and potential defects in the final product. The sticking of material on the plug's toe can result from various factors, including the type of material being pierced, lubrication effectiveness, and the speed at which the piercing process is conducted [6]. Researchers analyzed the internal crack during the seamless tube process with simulation and experimental scope. Pater et al. [7] simulated two roller piercing processes using the finite element method (FEM) and used a damage model to predict internal crack growth during the piercing process. They used Forge NxT 1.1. Software, 100Cr6 grade steel, and they mentioned the use of Cockroft-Latham damage model [8]. They stated that the damage model could predict the internal crack. Topa et al. [9] simulated the seamless tube piercing process of Plasticine steel with arbitrary Lagrangian–Eulerian (ALE) formulation in LS-DYNA software. They investigated the material behavior during the simulation and did not present any physical phenomena regarding the material they used. Joun et al. [10] investigated the Mannesmann effect by the finite

* Corresponding author.
E-mail address: h.aghajani@deusto.es (H.A. Derazkola).

https://doi.org/10.1016/j.rineng.2023.101682
Received 26 October 2023; Received in revised form 5 December 2023; Accepted 12 December 2023
Available online 17 December 2023

Table 1
Chemical composition of Super Cr13 martensitic stainless steel.

Element	C	Cr	Ni	Mn	Si	Mo	Ti	V	Fe
Wt.%	0.03	11.5–13.5	4.5–6.5	0.5	0.5	1.5–3	0.01–0.5	0.5	Bal.

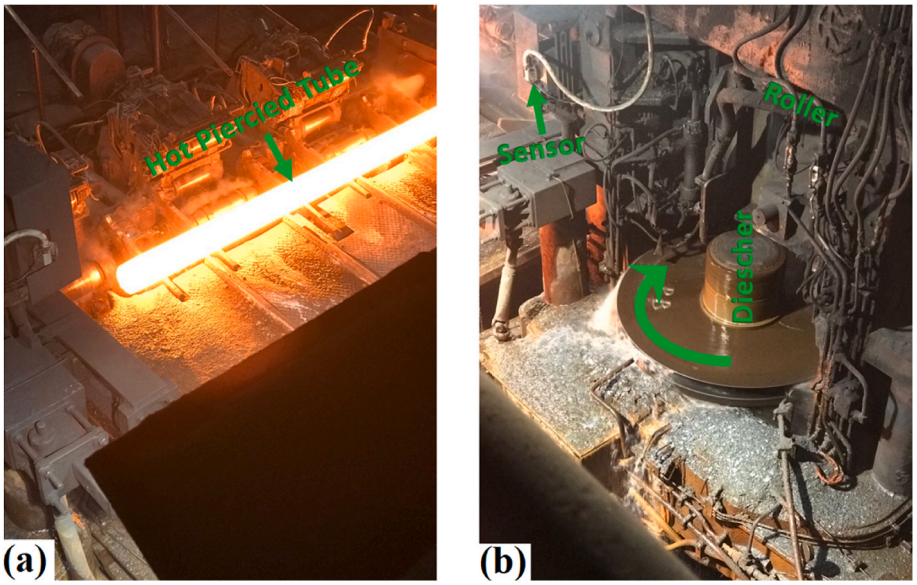

Fig. 1. (a) Picture of piercing process image and (b) hot tube after piercing.

element method during the piercing process. They used pure mechanical viewpoint simulation to analyze stress and strain rate at the tip of the plug. Lu et al. [11] used the finite element method to simulate Mannesmann effects during the piercing process. They used C45 steel material behavior during the simulation. In their results, the stress, strain, and material velocity were considered at the plug's tip, and they did not validate their results with experimental tests. The available research that connects the simulation results with experimental results for Mannesmann effects during seamless tube piercing is limited. Fanini et al. [12] were early researchers that planned to analyze material during the Mannesmann effect. Due to the complexity of this process, they used laboratory scale test campaign to find the fracture initiation at high temperatures. They stated that the fracture could not be considered a pure ductile fracture at a very low strain rate, and the fracture surface analysis showed intergranular fracture at a low strain rate. They used scanning electron microscope (SEM) images from the fractured tube in an actual piercing process and simulated the tube piercing with Cockroft & Latham, Oyane, and Lemaitre damage criteria [13]. According to their simulation, a predicted damage distribution by Cockcroft & Latham model had good agreements with experimental data [14]. Zhang et al. [15] investigated the effects of Mannesmann on the nickel-based superalloy. They simulated the piercing process with the finite element method and analyzed the crack initiation and growth during the piercing process. They stated that plastic deformation promotes by maximum shear stress. The maximum shear stress leads to microcrack initiation, and the maximum normal stress induces the internal voids generation of microcracks expansion. According to their results, the applied normal stress on the billet created the internal cracks, and for this reason, the hot tensile test can be a good approach for Mannesmann effects analysis. According to the available literature, various aspects of the Mannesmann effects are unclear.

First, the relation between material properties on crack initiation and growth is not clearly understood.

Second, what is the fracture morphology of billet materials during high-temperature during piercing process.

Previous researches were mainly focused on process simulation, and only Zhang et al. [15] and Fanini et al. [12] evaluated the simulation results with experimental results. On the other hand, effects of process parameters on the fracture of raw material have not been considered, previously. One of the primary process parameters is friction at interface of the tools-billet. Also, it is necessary to find the relation of the microstructure of raw material with Mannesmann effects and fracture analysis. For this reason, the piercing process of a super Cr13 stainless-steel tube is considered in this article. The effects of the tool-workpiece material behavior on the geometrical deviation, microstructure changes, and fracture of super Cr13 are investigated in this paper. The finite element method is used to simulate the piercing process, and experimental data is used to validate the simulation results.

2. Materials and methods

The experimental procedure in this study was conducted in two different steps. The first one consists of experimental tests carried out in the industry and the actual piercing process. The second phase of the experimental procedure is the determination of material ductility behavior by means of laboratory hot tensile tests to under controlled conditions. Investigating material behavior in the laboratory with controlled conditions provides valuable information that is hard or impossible to obtain in an actual situation. The results of both experimental tests (the laboratory test and industrial information) are related and have a meaningful connection. In this section, the details of the various testing procedures are presented separately. The term "plasticity" in the context of materials science is often associated with the ability of a material to undergo deformation without rupture or fracture [16]. In the case of steels, the temperature at which they exhibit the maximum plasticity is often referred to as the peak temperature for ductility or plasticity. The peak temperature for plasticity in steels can vary depending on the specific type of steel, its composition, and other factors. For type 13Cr steels, which are often a type of martensitic stainless steel containing about 13 % chromium, the temperature at

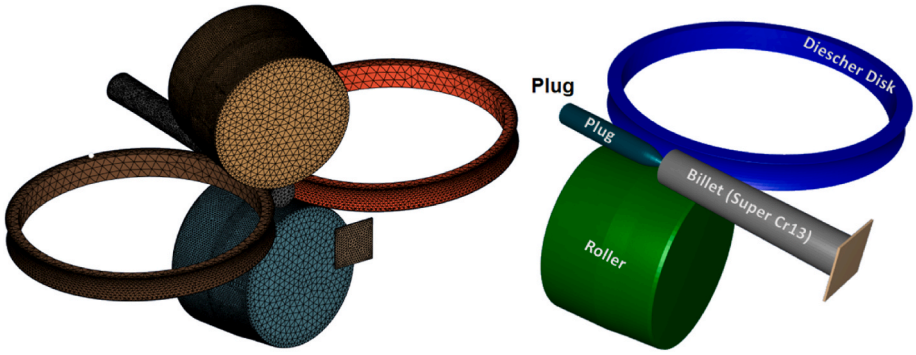

Fig. 2. (a) Meshed piercing process domain, (b) a view of piercing process tooling system.

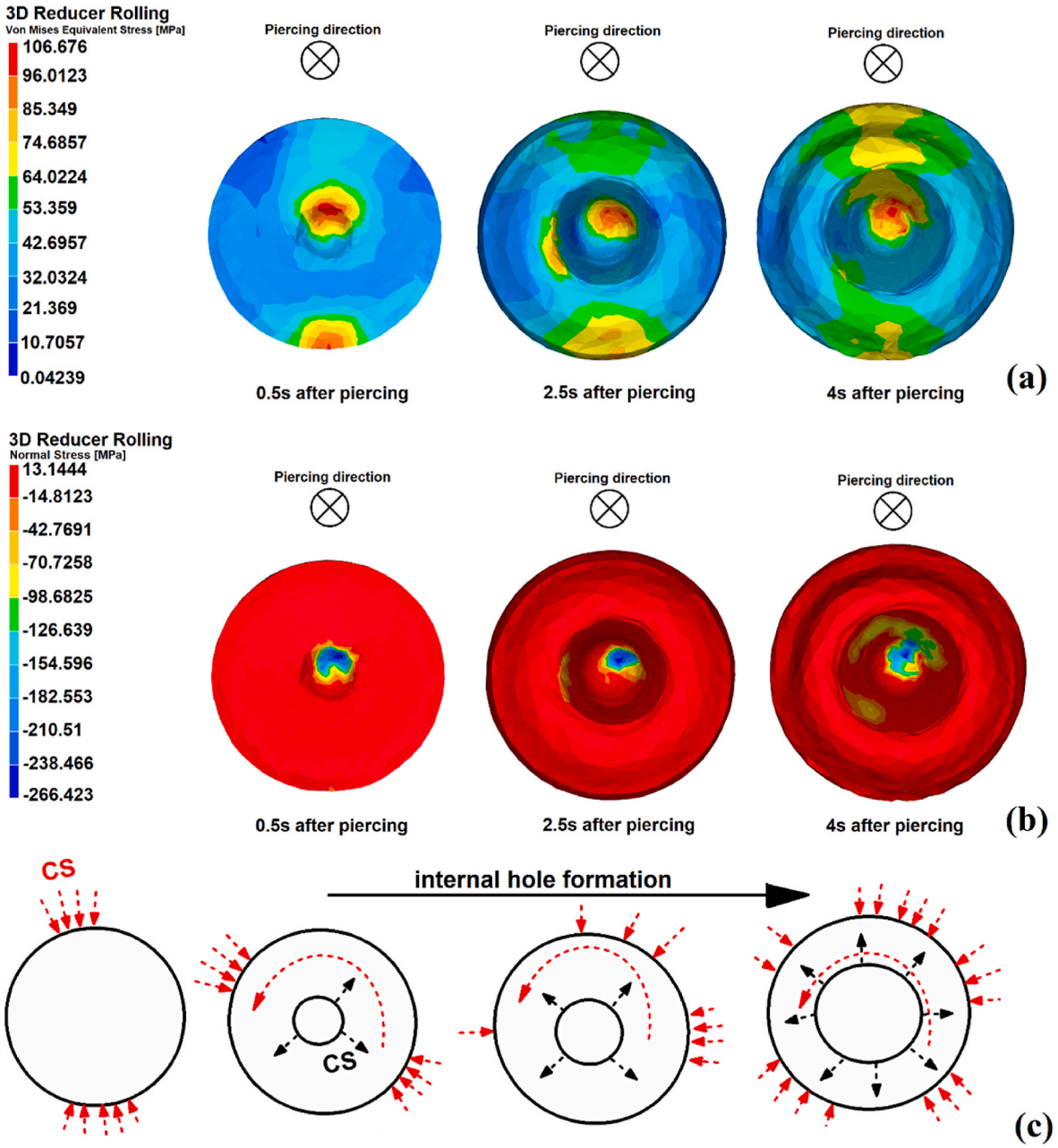

Fig. 3. Simulation results of (a) Von-Mises equivalent stress and (b) normal stress distribution on the sample at steps, 2, 6 and 9, (b) Schematic view of surface and internal stress direction on the sample at steps, 2, 6 and 9.

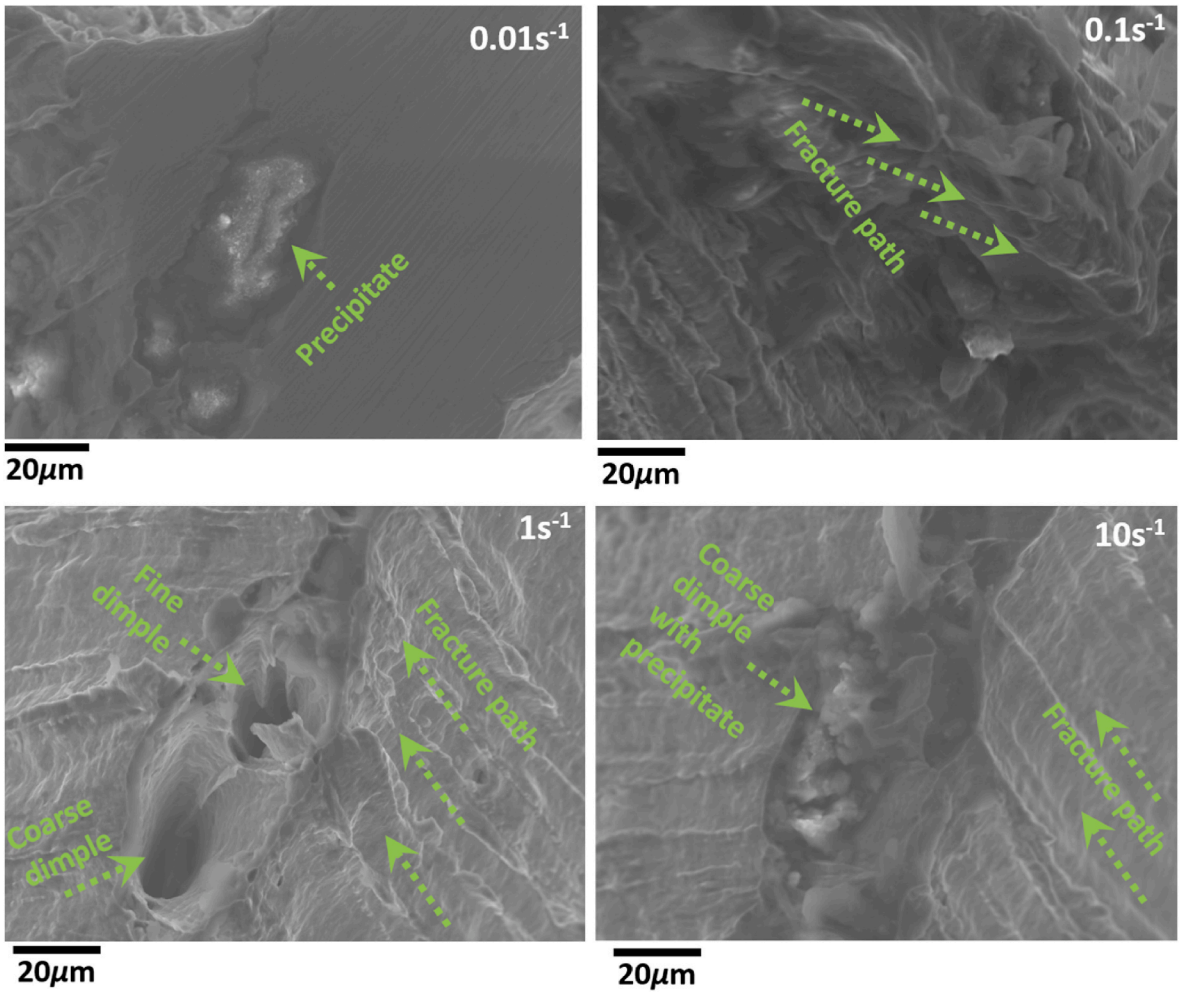

Fig. 4. SEM image of fracture surface of samples tested at $0.01s^{-1}$, $0.01s^{-1}$, $1s^{-1}$, and $10s^{-1}$.

which peak plasticity occurs can be influenced by factors such as alloying elements, heat treatment, and testing conditions, while in general case, the peak temperature for plasticity is in 650 °C till 700 °C range [17].

2.1. Seamless tube piercing process

The seamless tube piercing process was carried out in a real manufacturing factory. The piercing process procedure was carried out by Tubos Reunidos company. In this procedure, the super Cr13 martensitic stainless-steel billet was heated up to 1250 °C in a furnace and transferred into the piercing machine. The chemical composition of used super Cr13 stainless steel in this study is presented with Table 1.

At the beginning of the process, the billet temperature is 1250 °C; after it is cooled down by heat transfer with air and tolling system and thus, the temperature of the hot billet at the contact area with the tooling system decreases to 1100 °C. The super Cr13 stainless-steel billet had a 202 mm diameter and 1030 mm length. During this procedure, two Roller piercing machine was employed. The diameter of the Rollers was 940 mm with 111 rpm rotational speed. The rollers had 2° profile angles, 0° cross angles, and 10° feed angles. Two Dieshcher disks with a 210 mm radius were placed on the sides of the tube to control the geometry of the pierced tube. During the piercing process, the diameter of pierced section, thickness, and length of the tube was monitored by non-contact sensors, and Pyrometer recorded the surface temperature of the tube. The electrical consumption of rollers was recorded, and the information was used to validate simulation results. The simulation procedure is reported in the next section. A picture of the piercing machine and hot pierced tube (Super Cr13 stainless-steel tube) are presented in Fig. 1a and 1b, respectively.

2.2. Material behavior

A hot tensile test was carried out to analyze the crack growth and chemical changes during the piercing process. As discussed, analyzing crack growth during the piercing process is very hard. Due to the complexity of the crack initiation inside the tube, in some cases, it is impossible to monitor or track the crack initiation at the tip of the plug in the piercing process. The reasons for this approach would be.

1 The tube in the middle of the piercing process cannot be evaluated because removing the tube is time-consuming, and the raw material cools in the air. In this phase, the surface of cracks may react with oxygen, and the surface analysis with oxidation cannot be analyzed.
2 The billet in the middle of the piercing process is hot; the opening of the tooling system increases the possibility of inducing plastic deformation on the cracks and also the bonding of hot steel with the surrounding tooling.

For this reason, the lab's precise, controlled hot tensile test could expose the real situation phenomenon. In this regard, a constant testing temperature (1100 °C) was selected to reproduce the actual situation. The hot tensile test was carried out at $0.01s^{-1}$, $0.1s^{-1}$, $1s^{-1}$, and $10s^{-1}$ strain rates. The hot tensile test procedure was carried out according to

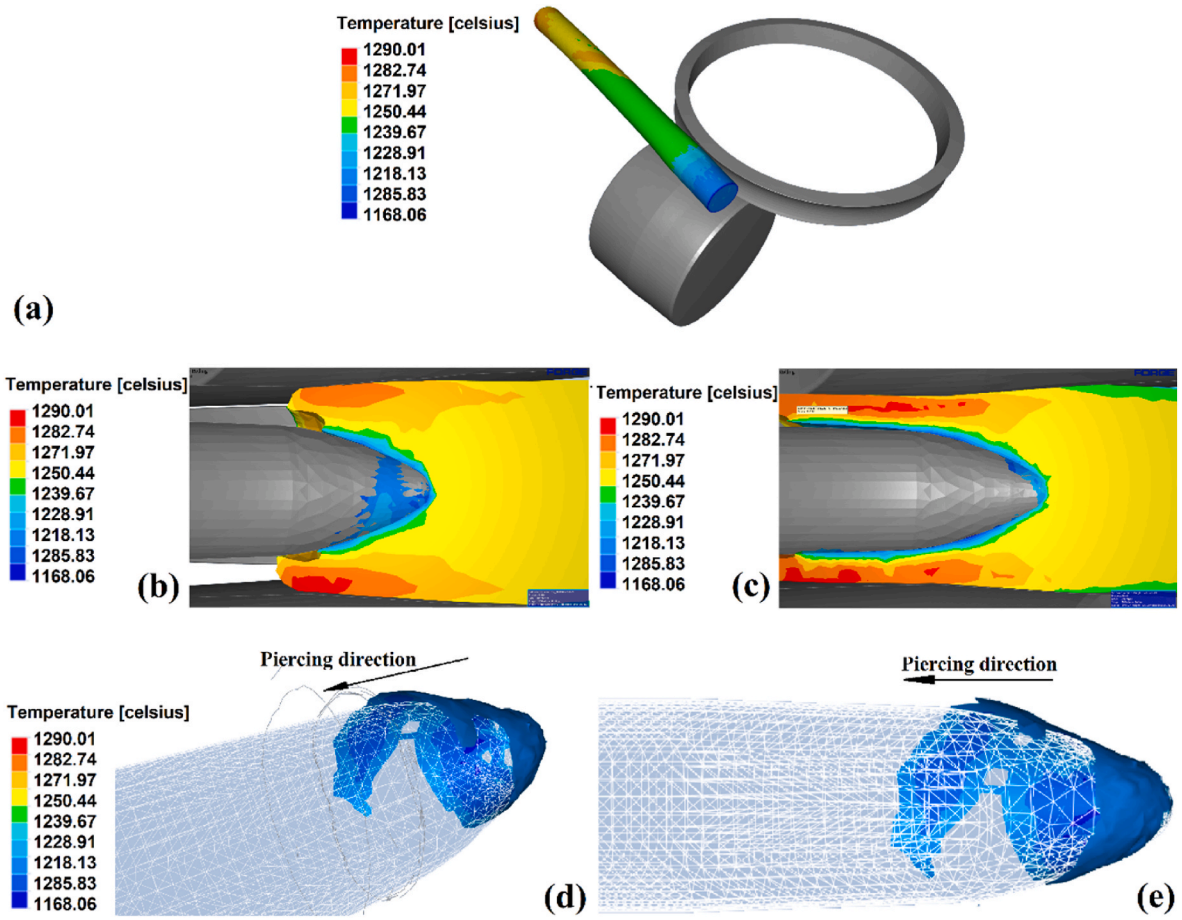

Fig. 5. Simulation results of temperature distribution on the tube (a) isometric view, cross section view of (b) early phase and (c) ending phase of piercing. 3D view of simulation results of (d) isometric and (e) side view of tube temperature at tip of plug.

the ASTM E21-09 (2020) standard [18], and the test specimens were prepared by ASTM E8/E8M (2021) [19]. The tested raw material was super Cr13 martensitic stainless steel (MSS), the same as pierced tube material. The chemical composition of super Cr13 martensitic stainless steel are presented in Table 1. The tensile sample cooled down in cold water (4 °C degrees) immediately after the test in order to freeze the microstructure of Super Cr13 and remove possible oxidation on the fracture surface. After the test, the fractured sample was washed with ethanol and prepared for characterization. The fracture surface of the sample was analyzed by scanning electron microscope (SEM) equipped with Energy-dispersive X-ray spectroscopy (EDS). The fractography of rapture samples was carried out using the ASTM C1322-15(2019) standard number. A sample from 3 mm below of fracture surface was cut, polished, and etched for microstructure evaluation based on ASTM E407 standard number. The microstructure was evaluated by optical microscopy equipped with image processing software.

3. Simulation procedure

The simulation of the process has been done by the finite element method (FEM). The software Forge NxT version 3.2 was employed to perform the process simulation. The dimension and geometry of all tools have been modeled based on actual dimensions. The model comprises two rollers, two Diescher disks, and a thrust bench. The tube material was selected as super Cr13 stainless steel with Hansel-Spittel constitutive law. The Hansel-Spittel constitutive law was adjusted based on the information provided by the supplier (Tubos Reunidos) [20]. Smooth surface contact was considered for billet-guide and billet-thrust bench, while friction contact was considered for roller-billet, Diescher disk-billet, and plug-billet interfaces. The details of the friction model, friction coefficient, and optimization process parameters have been reported by authors in a previous article [21]. Billet was considered a deformable component, and all tooling system parts were considered rigid bodies. A picture of meshed domain and tooling system is presented in Fig. 2a and b, respectively.

4. Results and discussions

4.1. Crack initiation inside tube

The simulation results, as depicted in Fig. 3a–b, provide a comprehensive front view of the impact of applied stress on the billet at various time intervals: 0.5, 2.5, and 4 s into the process, denoted as steps 2, 6, and 9, respectively. These temporal increments showcase the dynamic evolution of the tube piercing process, elucidating the transition from the initial stages to the establishment of a stable state during the piercing phase. The application of stress is strategically orchestrated at both the top and bottom regions of the billet, facilitated by rollers and a plug [22]. The upper and lower rollers come into contact with the hot billet in the top areas. As the billet moves forward, the plug initiates the piercing process. This phase concentrates stress around the pierced hole, compelling the compression of the hot material towards the exterior regions. As the piercing progresses, the tube wall undergoes a transformative journey, transitioning from a cylindrical shape to a tubular form. Notably, the simulation results highlight that the maximum Von-Mises equivalent stress applied to the billet reaches approximately 106 MPa. This stress is predominantly concentrated around the billet, indicative of the intense forces at play during the piercing process [21].

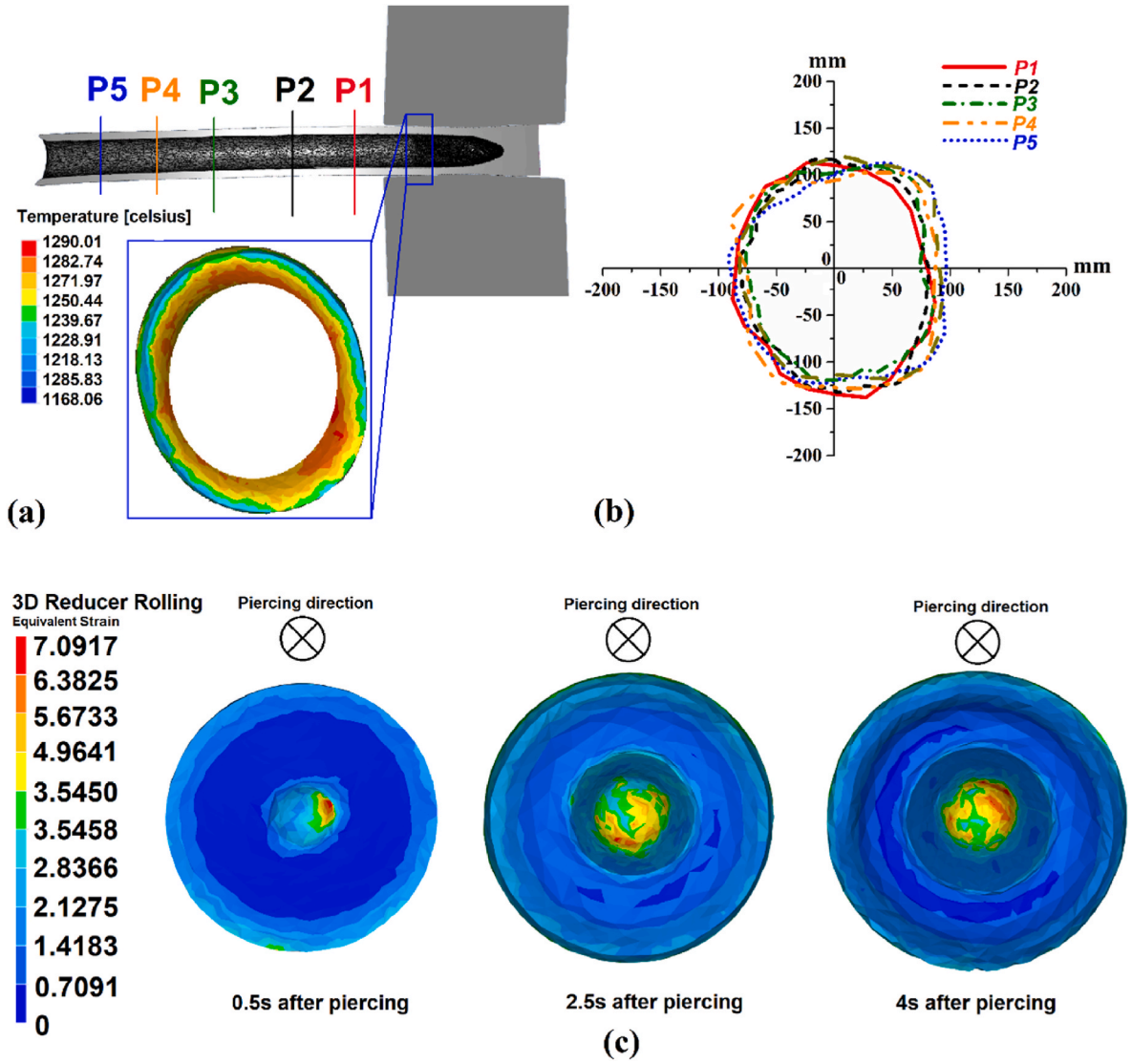

Fig. 6. (a) Sectioning view of pierced tube and (b) simulation results of tube perimeter geometry. (c) Simulation results of equivalent strain at various piercing steps.

In this simulation, distinct regions of normal stress distribution were observed in the front view (Fig. 3b). Notably, positive circumferential stress manifested itself in the hook direction of the tube, while negative circumferential stress was detected at the tip of the plug and billet interface. The positive stress values indicated tension, whereas negative values signified compression stress. The maximum circumferential tension stress reached 13.14 MPa, underscoring the substantial mechanical forces at play during the piercing process. Conversely, the maximum circumferential compression stress was predicted to be −266.423 MPa, revealing a significant degree of compressive forces acting on the tube. The analysis of circumferential compression stress shed light on a concurrent piercing and twisting motion of the tube [23]. This simultaneous motion suggests a dynamic interplay of mechanical forces contributing to the intricate evolution of the pierced tube. The negative circumferential stress concentrated at the interface between the plug and billet hints at localized compression, possibly influencing the material's plastic deformation (Fig. 3c). The simulation results elucidate the nuanced mechanical dynamics inherent in the seamless tube piercing process. The tension and compression stresses, coupled with the observed piercing and twisting motion, underscore the complex interdependencies shaping the tube's deformation during the manufacturing process [16].

The main factor in piercing is related to the crack initiation and crack growth inside the tube. This phenomenon is not similar to all materials. Due to the material used in this study (super Cr13 martensitic stainless steel), the fracture properties of tube material at 1100 °C and various strain rates were analyzed. The fracture surfaces of Super Cr13 MSS after hot tensile tests carried out at $0.01s^{-1}$, $0.01s^{-1}$, $1s^{-1}$, and $10s^{-1}$ are presented in Fig. 4.

The sample tested at $0.1s^{-1}$ showcased a rough fracture surface, implying a different fracture mechanism compared to the lower strain rate. The roughness of the fracture surface suggests a deviation from the formation of precipitates, pointing towards an altered deformation behavior under this specific strain rate condition. At a strain rate of $1s^{-1}$, the fracture surface presented a unique combination of fine and coarse dimples, coupled with a parallel fracture path [24]. This intricate morphology indicates a dynamic fracture process, suggesting that the material responded to the intermediate strain rate by displaying multiple fracture features. The coexistence of fine and coarse dimples implies a heterogeneous deformation response, possibly arising from localized variations in stress distribution within the material. The sample subjected to the highest strain rate, $10s^{-1}$, exhibited coarse dimples on the fracture surface along with the presence of precipitates and a parallel fracture path. This outcome suggests a distinct fracture mechanism compared to the other strain rates [25]. The coarseness of the dimples, coupled with the presence of precipitates, signifies a complex

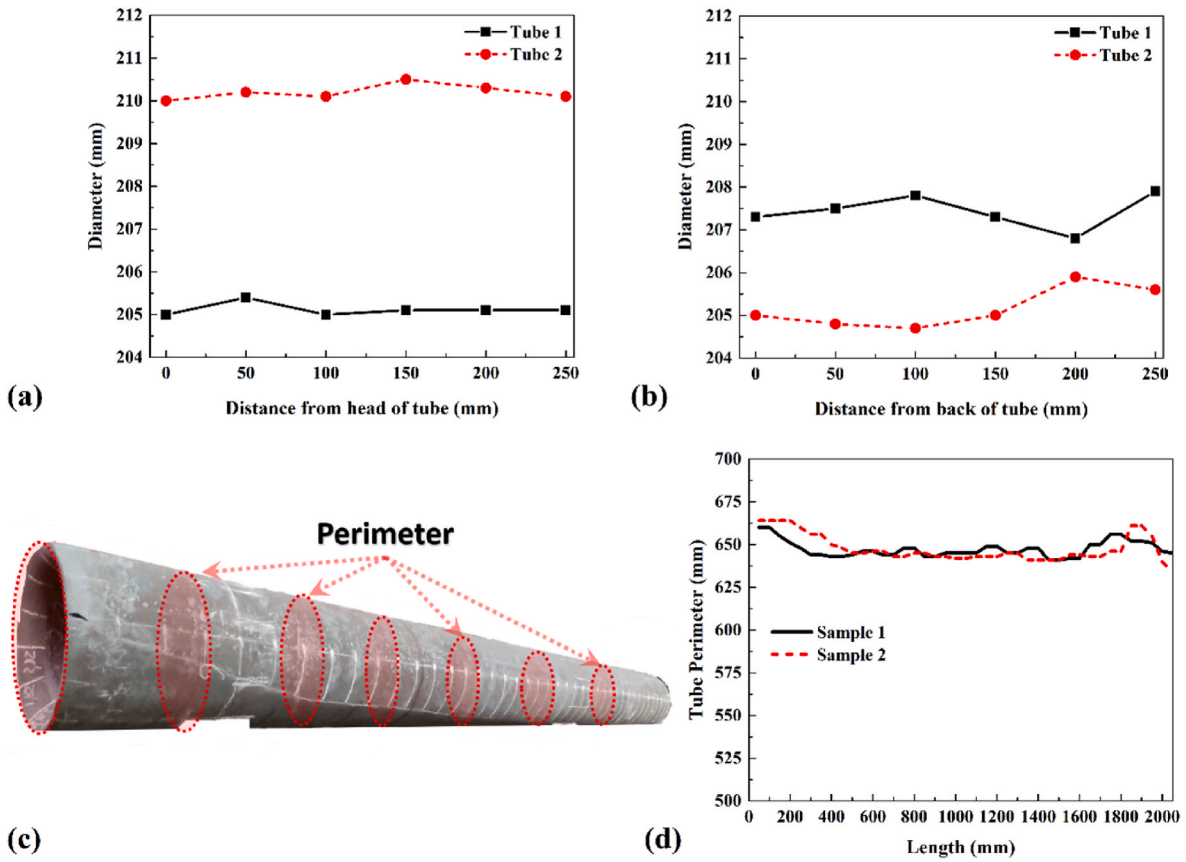

Fig. 7. Measured diameter of pierced tube form (a) head and (b) tail. (c) Picture of pierced tube with perimeter sectioning. (d) Experimental results from average tubes perimeter along the length.

interaction between strain rate, microstructure, and deformation behavior. The formed precipitate size at a low strain rate is more significant than at a high strain rate. The point, in this case, is that the precipitates in super Cr13 martensitic stainless steel are carbides, almost more rigid than steel matrix. These results indicate that the precipitates increase the hardness and shear strength of hot metal, consequently increasing the flow stress and decreasing the hot tube's formability. On the other hand, the high strain rate fracture surface indicates a mixture fracture (ductile + brittle) surface. The mixture fracture surface indicates the material piercing is not uniform in high strain rate and made antisymmetric tube geometry.

4.2. *Internal fracture effects on tube geometry*

During the piercing process, the temperature of the billet plays a leading role in the deformation of raw material. The simulation results of temperature distribution on the tube's external area and the tube's internal area at the early and end stages of piercing are presented in Fig. 5a, b, and 5c, respectively. The notable point from the simulation results is that after heating the billet in a furnace to start the piercing process, the billet's temperature decreases, and increases after piercing. This range of decrease and increase in temperature is not high. Due to the transfer of the billet with surrounded air (environment) and heat transfer with the tooling system, a hot billet temperature decreases during the pricing process. The results show that after the tube's piercing and due to plastic deformation, the temperature of pierced billet increases again. From the practical point of view, the surface heat of the pricing tube can be obtained (in a real production line in the industry, the surface heat of the piercing tube can be recorded), and the internal heat of the tube at the tip of the plug is hardly measurable. In this study, the internal temperature at the tip of the plug and hot super Cr13 stainless steel is not measured.

For this reason, it is decided to use FEM simulation results benefits to reproduce real thermo-mechanical situations at the tip of the plug during hot tensile test. The elastic, plastic, and friction power influenced the contact temperature in this case. As can be seen in Fig. 5d–e, the contact temperature at the tip of the plug barely reached 1163 °C. To reproduce the realistic fracture situation during the internal rapture of Super Cr13 stainless steel, a maximum of 1100 °C was selected for the hot tensile test. In this case, a better understanding of Mannesmann's effects can be reached on a laboratory scale by controlling the fracture initiation and growth. The changing temperature during the piercing process affects the geometry of the tube. According to obtained results, the minimum temperature of the billet was 1163 °C, and the temperature increased after plastic deformation [26].

A section from the pierced tube is depicted in Fig. 6a. The meticulous analysis of the simulation results revealed intricate details regarding the pierced tube's behavior along its length. The primary consequence of temperature fluctuations manifested in the eccentric formation of the pierced tube, introducing a distinct asymmetry to its overall geometry. This temperature-induced eccentricity emerged as a critical factor influencing the subsequent deformation patterns. Upon closer inspection, the cross-sectional view of the pierced tube exhibited a noteworthy departure from perfect circularity. To gain deeper insights, the pierced tube was systematically divided into five distinct sections denoted as P1, P2, P3, P4, and P5, allowing for a granular examination of its geometric evolution. Strikingly, the exterior profile geometry across all these sections consistently defied circular norms, portraying a complex and non-uniform deformation process (Fig. 6b). Further scrutiny of the sectional geometries derived from P1, P2, P3, P4, and P5 unveiled not only non-circular shapes but also distinct variations and discrepancies among them. This diversity in sectional geometries underscored the dynamic

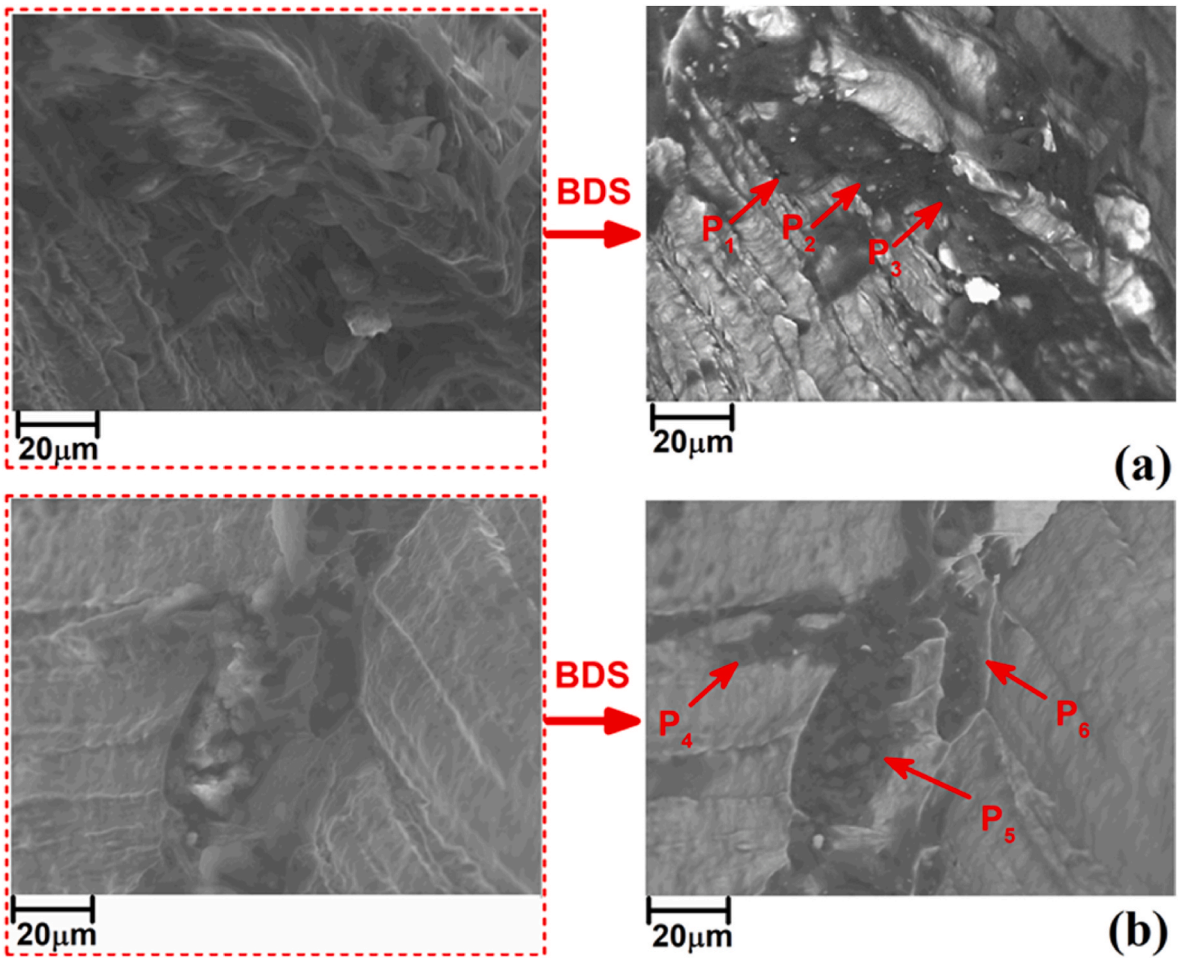

Fig. 8. BDS-SEM image from fracture surface of samples tested $0.01s^{-1}$ and $10s^{-1}$ with precipitates prospective.

and variable nature of the deformation process during piercing, suggesting that multiple factors contribute to the nuanced outcomes observed [27]. A compelling observation emerged from the consistent leftward expansion of the pierced tube across all sections during the piercing process. This uniform directional trend in expansion hinted at a cohesive and orchestrated deformation mechanism, likely influenced by specific mechanical forces acting asymmetrically on the tube [28]. Delving into the equivalent strain results, a noteworthy pattern emerged, with the tip of the plug experiencing significantly higher equivalent strain values than other areas. The maximum equivalent strain, quantified at 7.0917, localized specifically to the left side of the plug. This pivotal finding implicated the left side as a focal point for crack initiation, growth, and hole formation, shedding light on the critical role of localized strain concentrations in shaping the final structural integrity of the pierced tube (Fig. 6c).

The experimental results of pierced tube geometry are depicted in Fig. 7. During the experimental tests two tubes were pierced as samples. The pierced tube was evaluated, and the results were presented. The diameter of the tubes was measured from the head from 0 mm (tube head tip) to 250 mm, and the tail of the tubes from 0 mm (tube tail tip) to 250 mm was measured, and the statistic results are presented in Fig. 7a–b. In this section, the average diameter of pierced tubes is presented. The experimental results revealed that the mean diameter of the pierced tubes at the head was 208 mm, while the initial cylinder (billet) had 201 mm diameter with uniform shape. The results indicated that the mean value of pierced tube diameter was 206 mm at the tail. The average tube diameter in FEM simulation was 210 mm. Fig. 7c shows a picture of a pierced tube. To evaluate tube geometry, the perimeter of pierced tubes was measured, and the results are presented in Fig. 7d. The results of perimeter measurements show that the perimeter of the pierced tube is not uniform along the length. As can be seen, the collected data from different points of the tube presented in Fig. 7d are not straight lines. It means that the perimeter of the pierced tube along of tube is not the same and is not uniform. In some areas, the perimeter is bigger than in other areas. The most fluctuation in perimeter can be seen in the tail and head of the tube.

As the results revealed, the exterior area of the pierced tube is not perfectly cylindrical shape nor uniform along the tube. It can be concluded that the simulation results had good agreements with experimental results. Due to obtained results, the mean value of pierced tube perimeter is 660 mm, while the mean value of the tube perimeter in the simulation was 675 mm.

Simulation and experimental results put into evidence that, from a manufacturing point of view, the material deformation is not homogeneous given the differences found in the analyzed geometry of the tube. It could be explained by the metallurgical changes inside and outside the hot billet during the piercing process, which can affect the material behavior. As discussed before, the strain rate can modify the tube's fracture behavior. The fracture analysis shows that the precipitates are formed on the fracture surface at a lower strain rate. An example of a BDS-SEM image of the fracture surface of hot tensile test samples tested with $0.1s^{-1}$ and $10s^{-1}$ are presented in Fig. 8a–bfig8, respectively. The results show that precipitates locally cover the fracture surface. There are two points about the precipitates. First, the volume of precipitates at high temperatures is very low, and the amount of these precipitates is kinematically formed during the cooling stage of the broken sample.

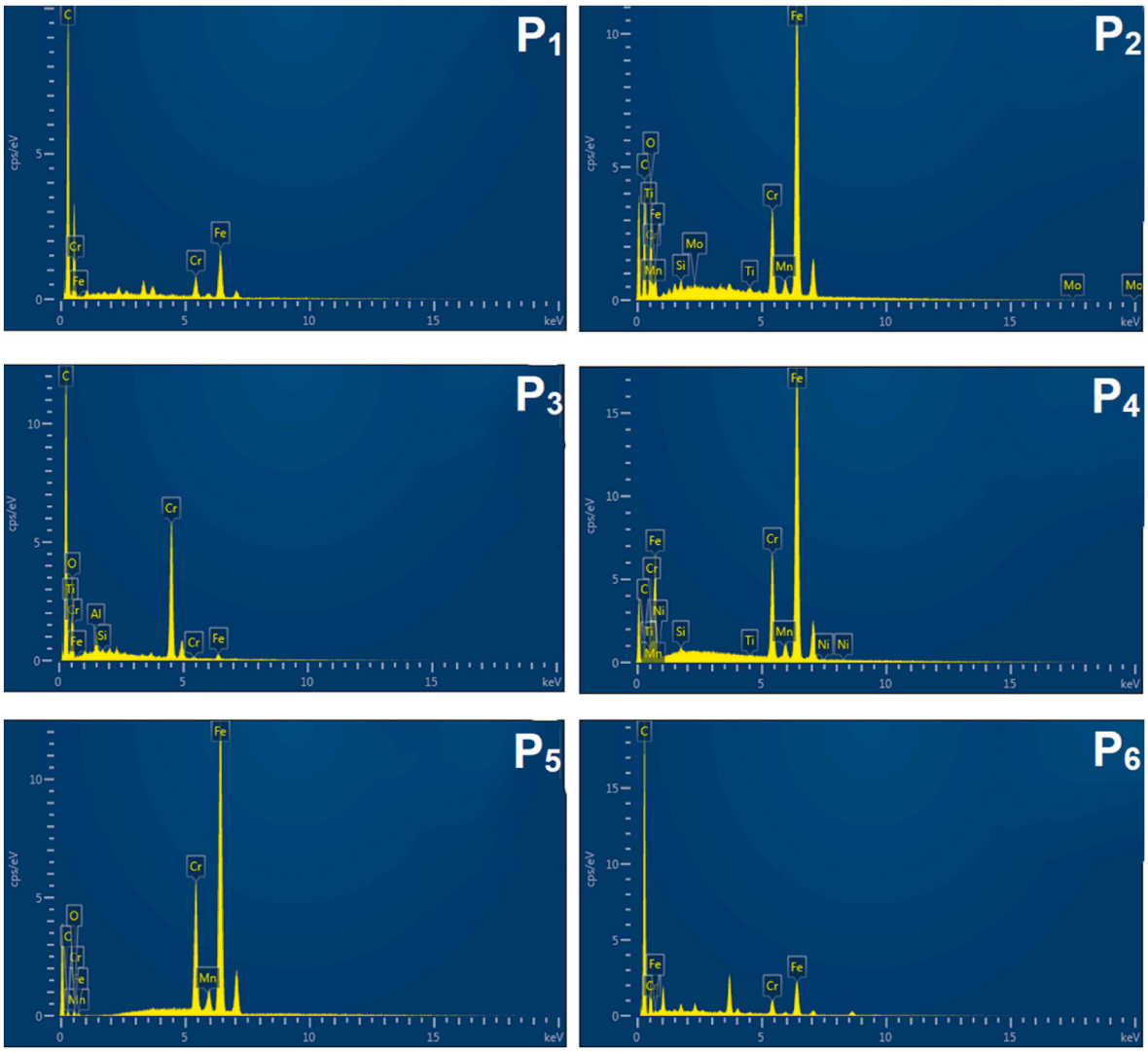

Fig. 9. EDS point analysis of points P_1, P_2, P_3, P_4, P_5 and P_6.

Second, the chemical composition of these precipitates is not uniform. The EDS point analysis of selected precipitates (points P1 to P6) is presented in Fig. 9. The chemical analysis indicates that these areas combine oxides, carbides, and Fe–Cr precipitates. The amount of oxide (shiny white points) is not high, and it is clear that the oxides were formed at the fracture surface during the cooling stage, when the sample was exposed to air. After the hot tensile test, the samples are immediately submerged into cool water to prevent formation of oxides. For this reason, the amount of these oxides is limited. On the other hand, as can be seen in the results, the formed precipitates are mainly carbides with an $M_{23}C_6$ chemical composition. These precipitates are common in super Cr13 martensitic stainless-steel microstructure—also, Fe–Cr and Fe–Cr–Ni precipitates are detected on the fracture surface.

The point is that the carbide precipitates can significantly affect the flow stress of Super Cr13 stainless steel. Generally, the carbides are compounds that form when carbon atoms combine with metal atoms, and they are typically harder and more brittle than the surrounding steel matrix. When carbides precipitate out of the steel matrix during an induced thermo-mechanical process or cooling treatment, they can create obstacles to dislocation motion, which can increase the flow stress of the super Cr13 stainless steel [29]. The size, distribution, and composition of the carbide precipitates can all influence their effect on flow stress. Larger carbides are generally more effective at obstructing dislocation motion than smaller ones, and their distribution throughout the steel can also affect the overall flow stress. The composition of the carbides can also be important, as different carbides can have different strengths and interact differently with the surrounding steel matrix. Generally, carbide precipitates in steel can increase its strength and hardness but can also make it more brittle. As simulation results show, the surface heat transfer with rollers and inside heat transfer with plug decrease the temperature of the billet. These temperature changes effects of flow stress of super Cr13 stainless steel, and as a result, the material behavior shows non-uniform deformation, which leads to an eccentric geometry in the final tube.

5. Analysis of tube thickness

The thickness of a pierced tube is a geometry factor that forms after the hot forming process. The uniform process can lead to uniform thickness values along the tube, and guarantees the homogeneous function of the tube after production [30]. During the piercing process, the rollers applied normal force, and the stretching of hot metal formed an internal crack. The material behavior can determine the tube's geometry and the tube's thickness.

The internal flow of the material should be uniform at the upper and lower sides of the plug. If the internal crack growth is nonuniform inside the tube, the stretching of the hot material could be higher in the upper or lower area of the plug and, in this case, the formed tube's thickness

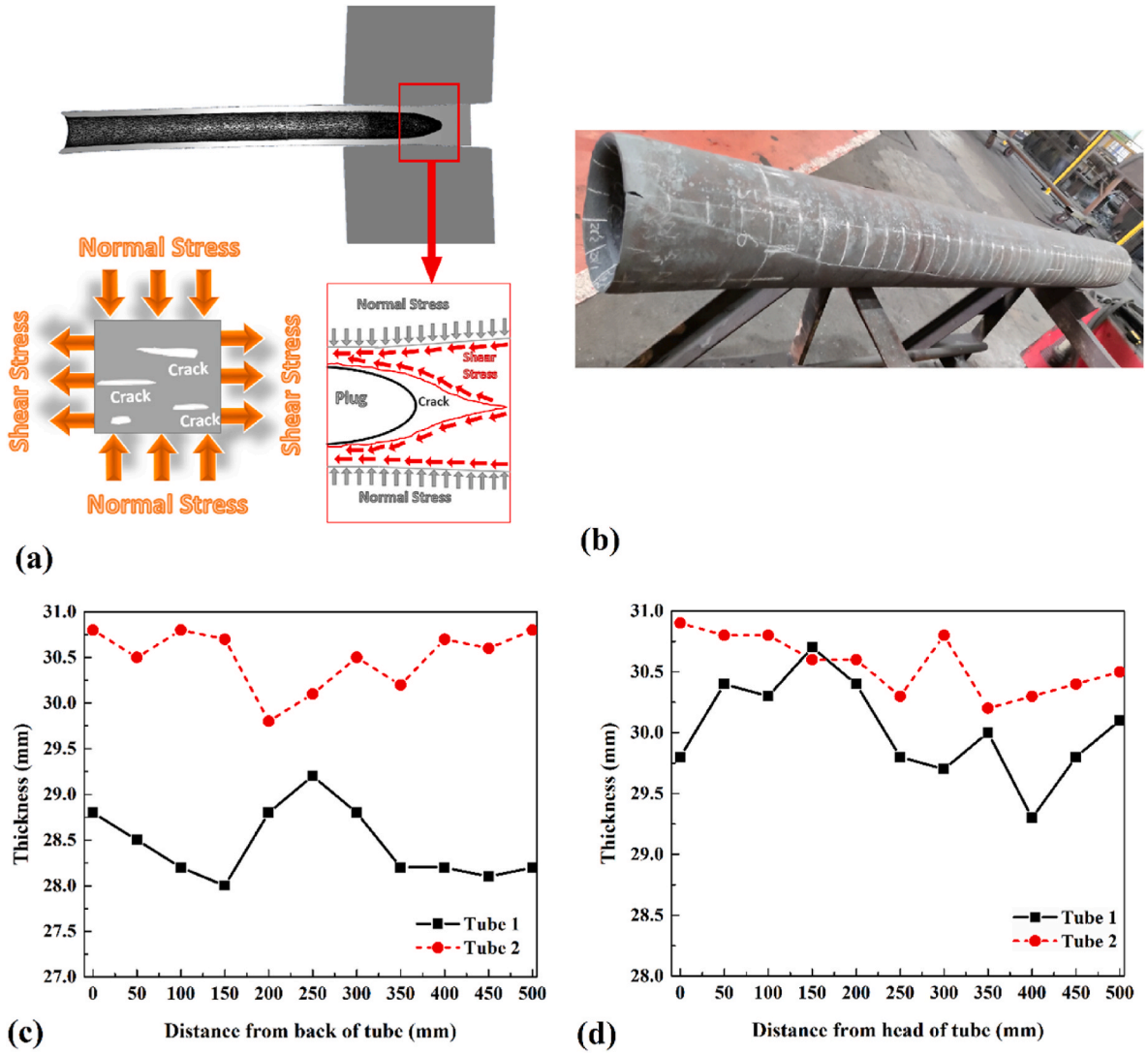

Fig. 10. (a) Schematic view of internal crack growth during piercing process. (b) Picture of pierced tube. Measured thickness of pierced tube form (c) head and (d) tail.

may be antisymmetric. The schematic view of internal stress state on the hot tube is presented in Fig. 10a. As it can be appreciated, the applied load by rollers and plug in front of the internal crack act as a tension test. A picture of the selected tube for thickness analysis is presented in Fig. 10b. The thickness of pierced tubes from the head and tail of the tube are presented in Fig. 10c–d, respectively.

The obtained results revealed that the thickness is not uniform along the pierced tube (similar to the perimeter). In this case the super Cr13 stainless-steel behavior can affect the direction of internal crack growth and modify the thickness of tube. According to obtained results, the mean thickness at the head of the tube was 29 mm, and at the tail was 30 mm. The volume of the initial billet before and after piercing is constant. The variation in perimeter and thickness are clues that the elongation of tube during piercing is not constantly uniform. On the other hand, it means that despite constant process parameters, the head of tube Stretched (elongated) more than the tail of tube. For this reason, the thickness of tube at tail of the tube was thicker than head. This phenomenon is inevitable and depends on raw super Cr13 stainless-steel behavior. The non-uniform behavior of super Cr13 stainless steel can also be detected by axis deviation analysis. The axis deviation is a technique for finding the surface deformation of raw material before and after piercing. The length of the billet at the early stage is shorter than the pierced tube. In this case, a normal axis of the raw billet is marked on the surface of the tube, and after piercing, the market area's displacements are connected. A picture of the super Cr13 stainless-steel axis deviation is presented in Fig. 11a. The length of deviations measured and the results are presented in Fig. 11b. The results revealed that the axis deviation is not constant along the tube length, being higher at the head of the tube than at the tail. The maximum axis deviation was measured at the head of the tube with 120 mm, and the minimum was at the tail of the tube with 20 mm. The simulation results of tube displacement are shown in Fig. 11c. The simulation result did not wholly match experimental results but showed the same trend of experiments. It means that the axial displacement of the tube at the head and tail was not constant.

6. Microstructure and fracture during piercing

During the piercing of the tube, the raw material is deformed at a high strain rate. Simulation results of applied surface strain rate, internal strain rate at the early step, and end last steps of the piercing process are presented in Fig. 12a, b, and 12c, respectively. The results indicate that the maximum strain rate on the tube is in the roller's contact area, and the strain rate at the peak of the plug is not very high. In this case, the peak of the plug tolerates a low strain rate, which increases the non-uniform fracture behavior of super Cr13 stainless steel. The average

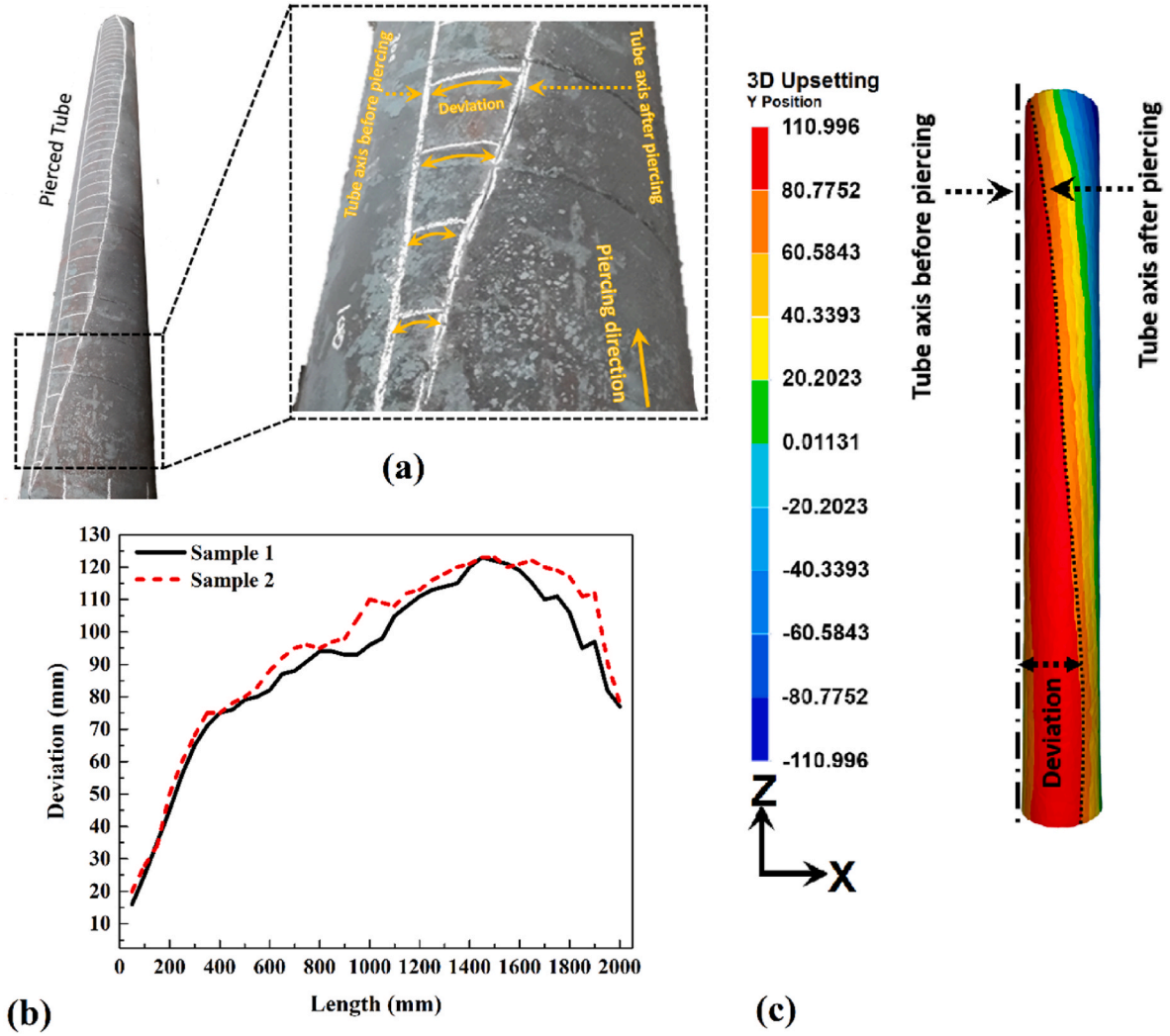

Fig. 11. (a) Picture of tube axis deviation. (b) Tube axis deviation along of length and (c) simulation results of tube axis deviation.

strain rate (in overall) is predicted between $5s^{-1}$ to $50s^{-1}$. The strain rate at the plug's tip differed from the rollers-billet contact area. The average strain rate at determined $10s^{-1}$. The strain rate can affect the fracture behavior of super Cr13 stainless steel due to changes in microstructure at high temperatures.

The microstructure of raw super Cr13 stainless steel at room temperature is depicted in Fig. 12d. The results show that the super Cr13 stainless-steel microstructure has δ-ferrite, retained δ-ferrite, austenite, retained austenite/ferrite (σ), and precipitates spread in martensite lath matrix. High-magnification optical microscopy images have recognized this microstructure at room temperature. The point is that during the piercing process, the super Cr13 stainless steel operates at temperatures higher than 1000 °C. Thus, super Cr13 stainless steel's microstructure differs from room temperature. According to the equilibrium diagram at temperatures higher than 1000 °C, the microstructure of super Cr13 stainless steel consists of δ-ferrite and γ-austenite. The microstructure analysis of hot tensile samples after the test at various strain rates ($0.01s^{-1}$, $0.01s^{-1}$, $1s^{-1}$, and $10s^{-1}$) are presented in Fig. 13a. The results show that the retained δ-ferrite in various samples has a different shape. The δ-ferrite in low-strain rate samples is small and thick (as seen in microstructure results), and elongated at a higher strain rate (as seen in the optical microscopic image).

As a first step, the mean size of δ-ferrite in the microstructure of hot tensile test samples is measured. During the hot tensile tests, all samples were heated up to 1100 °C and cooled down with the same procedure. Because the procedure followed on all tests was the same, it seems that the changes in microstructure are related to the differences in strain rate of the tests. Image processing software was used to measure the width and length of δ-ferrite at tensile samples, and the results are presented in Fig. 13b. As mentioned, the only phases in super Cr13 stainless steel are δ-ferrite and γ-austinite at a temperature over 1100 °C. Generally, the δ-ferrite is a soft phase compared to the surrounding matrix (austenite) at high temperatures. At high temperatures, the δ-ferrite originates crack initiations and growth [31]. According to the obtained results, with increasing strain rate, the thinner δ-ferrite remained in the microstructure of samples. As depicted in Fig. 13c, at a low strain rate, the δ-ferrite split slowly, and a local thick region of δ-ferrite can be detected in the microstructure.

A notable phenomenon in examining high strain rates emerges as the δ-ferrite undergoes internal rupture, resulting in accelerated fracture within the super Cr13 stainless steel. The intricate details of the fracture surface are unveiled through the BSD-SEM images of the tensile samples subjected to strain rates of $0.01s^{-1}$ and $10s^{-1}$, presented in Fig. 14a–b, respectively. These images encapsulate coarse and fine dimples, fracture path intricacies, and fracture width particulars, offering a comprehensive view of the material's response to varying strain rates. The fracture width at low strain rates is notably smaller than at high strain rates. This disparity indicates that the fracture growth is markedly swifter under high strain rates, irrespective of the applied load or strain rate during deformation. Intriguingly, it is inferred that the internal fracture within

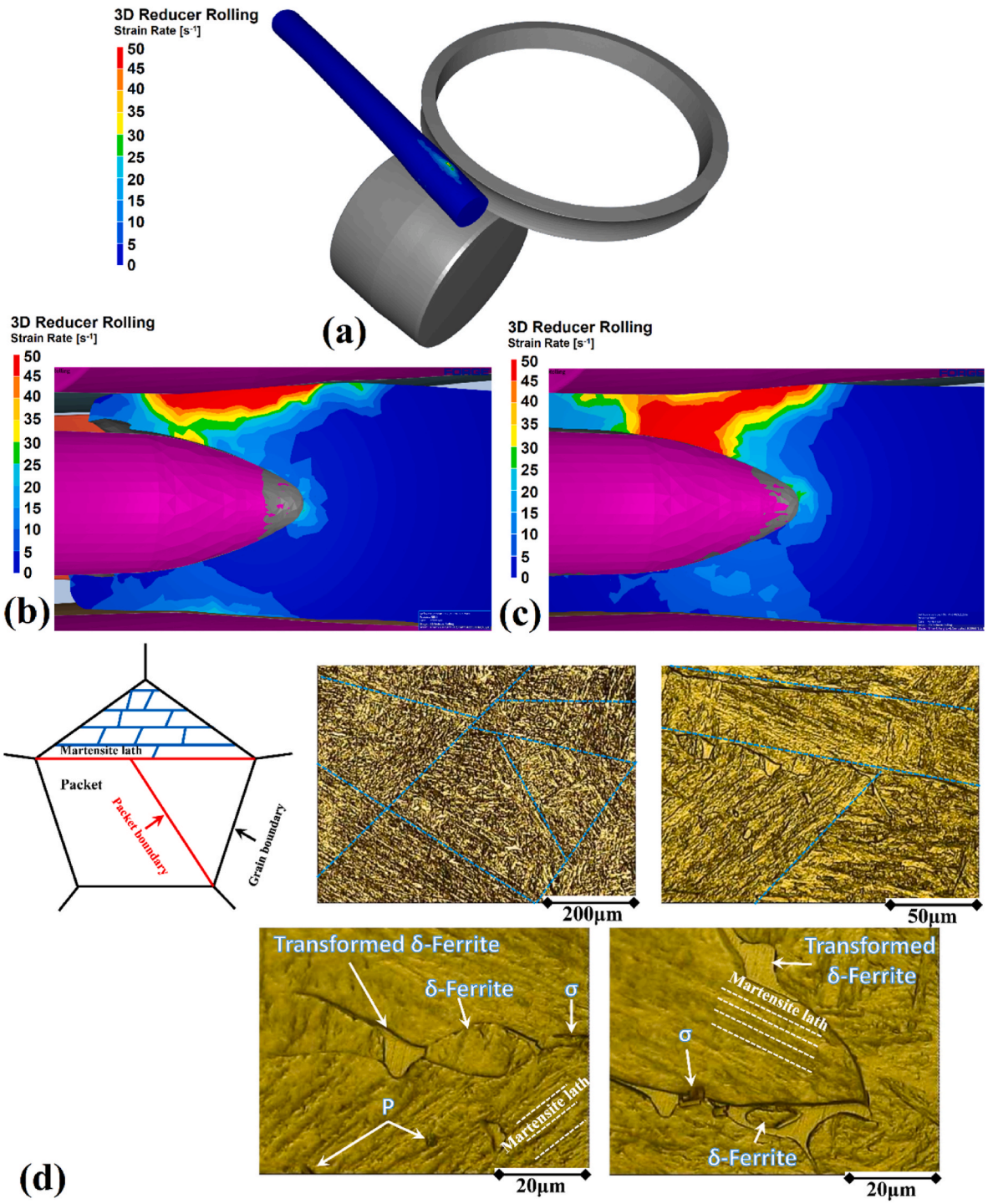

Fig. 12. Simulation results of strain rate distribution on the tube (a) isometric view, cross section view of (b) early phase and (c) ending phase of piercing. (d) Microstructure of super Cr13 stainless-steel at room temperature.

δ-ferrite plays a pivotal role in enhancing crack propagation speed, contributing to the observed rate-dependent fracture behavior. Moreover, the investigation into fracture path width reveals a correlation with the thickness of δ-ferrite observed in microstructure analysis.

This alignment implies that, at higher strain rates, the rupture speed increases, and the primary factor behind this heightened rupture velocity appears to be the splitting of δ-ferrite. These insights into the material's behavior hold significance in understanding the internal fracture dynamics of super Cr13 stainless steel during the piercing process. The study further elucidates that the size of δ-ferrite at the operational temperature for piercing exhibits non-uniformity. The variation in strain rates at the plug's tip during internal piercing results in localized occurrences of split ruptures in some areas and not in others. Consequently, the fracture behavior at the tip of the plug manifests as asymmetrical and non-uniform, contributing to the observed antisymmetric variations in tube thickness and perimeter. This nuanced understanding sheds light on the intricate interplay between material properties and dynamic deformation processes, enhancing our comprehension of the mechanical behavior of super Cr13 stainless steel in high-strain-rate scenarios.

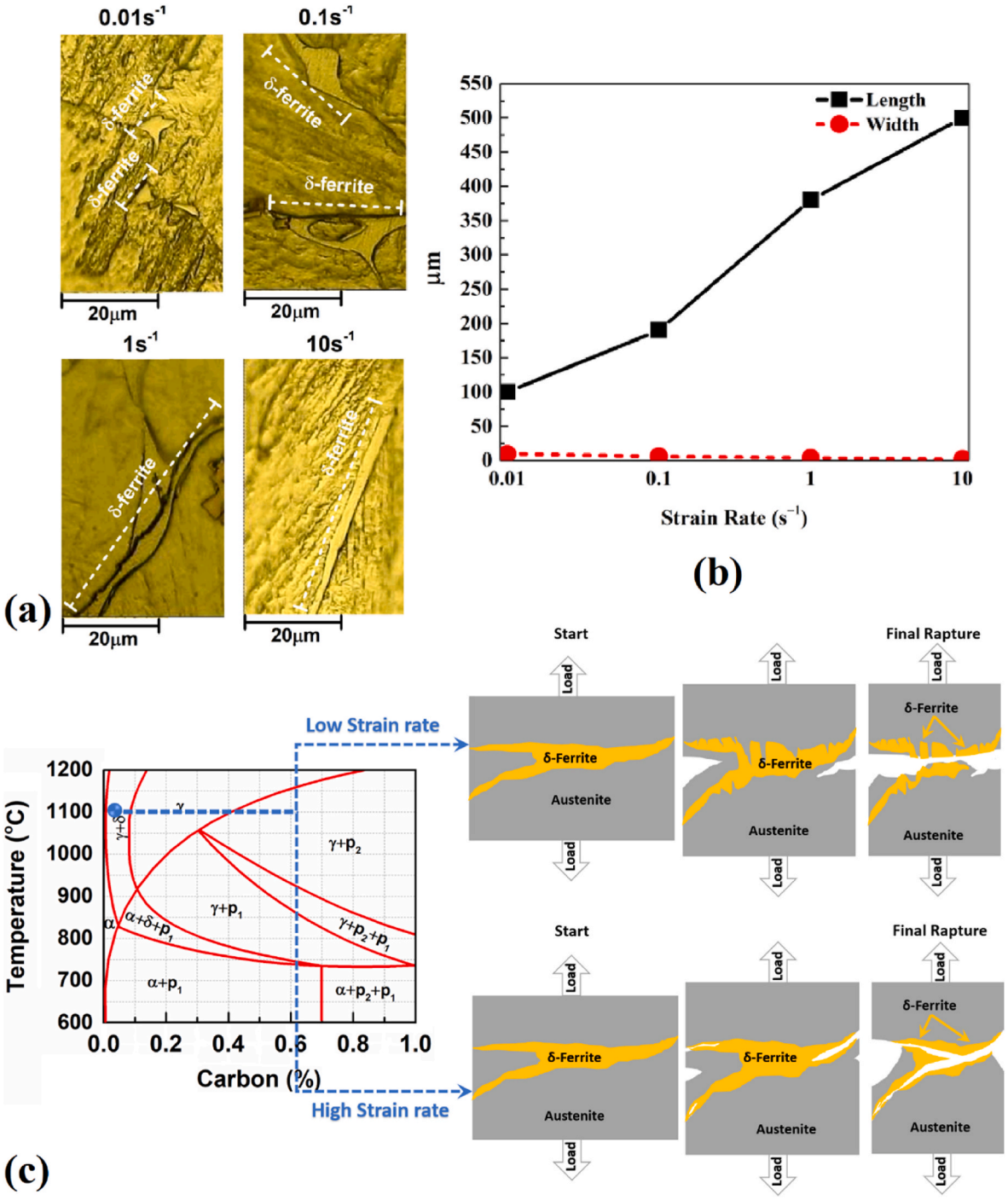

Fig. 13. (a) Geometry of δ-ferrite at the microstructure of various samples. (b) Average length and width of δ-ferrite. (c) Schematic view of strain rate effects on fracture of δ-ferrite at high temperature.

7. Conclusions

This study evaluates the relation between super Cr13 stainless steel behavior during piercing process with a geometric deviation of the pierced tube. The internal fracture of super Cr13 stainless steel during the piercing process is analyzed, and the archived conclusions are presented below.

1 Following the piercing process, the tube's perimeter and diameter exhibit deviations from perfect circularity. The non-homogeneity in deformation is attributed to variations in the flow stress of super Cr13 stainless steel during piercing. The experimental findings indicate a mean pierced tube perimeter of 660 mm, contrasting with the simulated tube perimeter of 675 mm. Moreover, the mean diameter of the pierced tubes at the head measures 208 mm, while the initial uniform cylinder (billet) had a 201 mm diameter. Notably, the mean diameter of the pierced tube at the tail is 206 mm, in contrast to the FEM simulation's average tube diameter of 210 mm.

2 Heat transfer interactions between the tooling system and the hot super Cr13 stainless steel result in the formation of hard precipitates, inducing local increases in flow stress and causing deviations in different axes of the produced tube. The obtained results reveal a

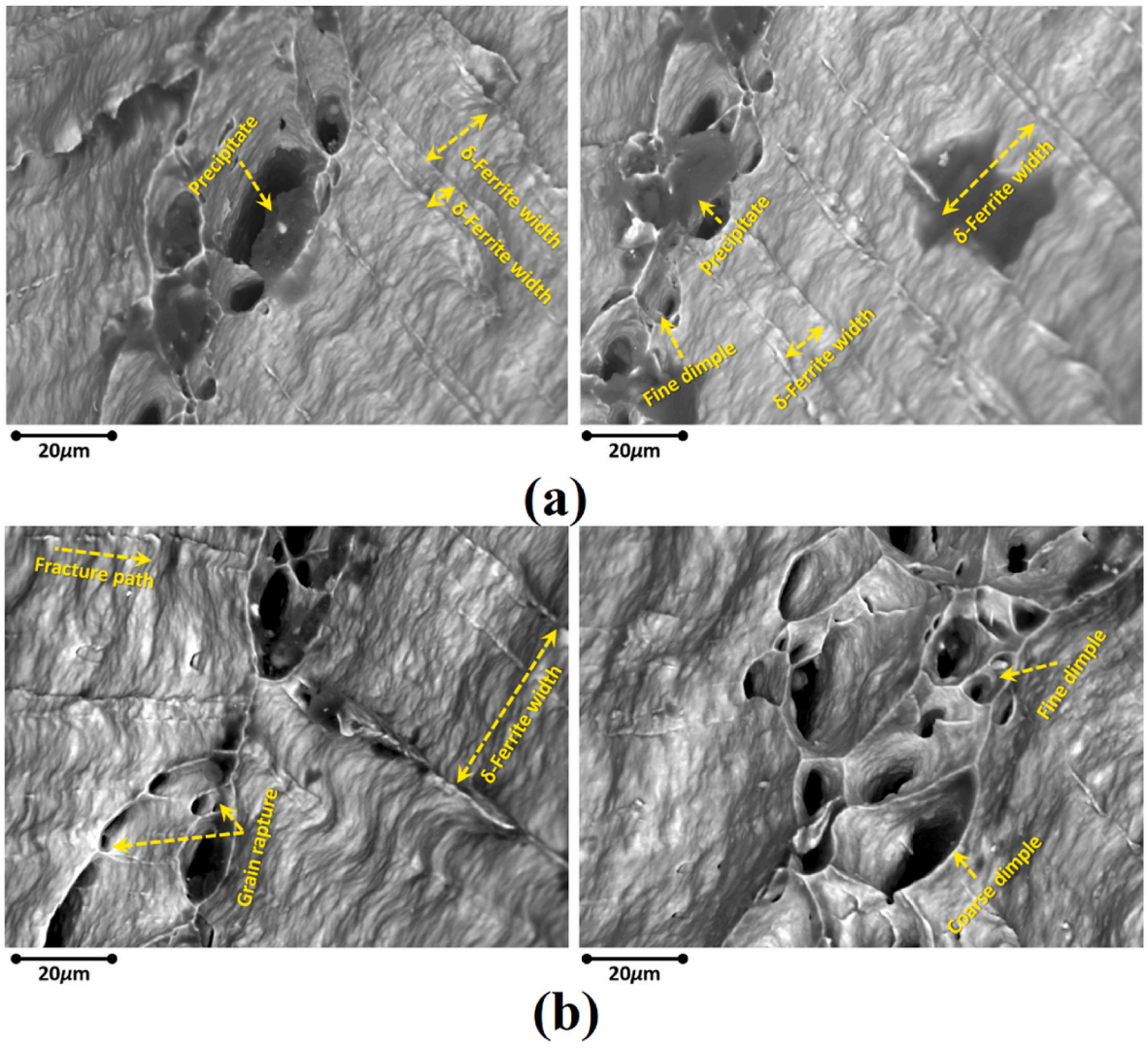

Fig. 14. BDS-SEM image from fracture surface of samples that tested with (a) $0.01s^{-1}$ and (b) $10s^{-1}$ with fracture path perspective.

contact temperature of 1100 °C at the plug's tip, contributing to internal fracture growth.

3 The non-uniform strain rate across the tube's cross-section during piercing leads to heterogeneous fracture growth at the plug's tip, subsequently influencing thickness variations at the head and tail of the pierced tube. The predicted average strain rate ranges from 18sˆ-1 to 70sˆ-1. The maximum axis deviation, measuring 120 mm, is observed at the head, while the minimum, at 20 mm, is observed at the tail of the tube.

4 The primary initiation of cracks in super Cr13 stainless steel at high temperatures occurs through the internal rupture of δ-ferrite. The fracture behavior of δ-ferrite at high temperatures, particularly at low strain rates, differs significantly from that observed at high strain rates. This discrepancy contributes to the fracture sensitivity of super Cr13 stainless steel at the plug's tip during the piercing process.

Funding

This project has received funding from the European Union's Horizon 2020 Research and Innovation Programme under the Marie Skłodowska-Curie grant agreement No. 847624. In addition, a number of institutions back and co-finance this project. The paper reflects only the authors' view and the Agency is not responsible for any use that may be made of the information it contains.

Institutional review board statement

Not applicable.

Informed consent statement

Not applicable.

CRediT authorship contribution statement

Hamed Aghajani Derazkola: Conceptualization, Formal analysis, Investigation, Methodology, Supervision, Validation, Writing - original draft, Writing - review & editing. **Eduardo García Gil:** Conceptualization, Funding acquisition, Project administration, Writing - original draft, Writing - review & editing. **Alberto Murillo-Marrodan:** Funding acquisition, Investigation, Methodology, Resources, Software, Writing - review & editing.

Declaration of competing interest

The authors declare that they have no known competing financial interests or personal relationships that could have appeared to influence the work reported in this paper.

Data availability

Data will be made available on request.

Acknowledgments

Not applicable.

References

[1] M.M. Skripalenko, et al., Simulation of the kinematic condition of radial shear rolling and estimation of its influence on a titanium billet microstructure, Materials 15 (22) (2022) 7980, https://doi.org/10.3390/ma15227980.
[2] J.M. Cho, B.S. Kim, H.K. Moon, M.C. Lee, M.S. Joun, Comparative study on Mannesmann roll piercing processes between Diescher's guiding disk and Stiefel's guiding shoe, AIP Conf. Proc. 1532 (1) (May 2013) 843–849, https://doi.org/10.1063/1.4806919.
[3] M. Fernandes, N. Marouf, P. Montmitonnet, K. Mocellin, Impact of the different friction coefficients on the tools on the mechanics of the mannesmann 2-roll tube piercing, ISIJ Int. 60 (12) (2020) 2917–2926, https://doi.org/10.2355/isijinternational.ISIJINT-2020-290.
[4] S.P. Galkin, Y.V. Gamin, T.Y. Kin, Analysis of temperature influence on strain–speed parameters of radial-shear rolling of Al-Zn-Mg-Ni-Fe alloy, Materials 15 (20) (Oct. 2022) 7202, https://doi.org/10.3390/ma15207202.
[5] A. Topa, D.K. Kim, Y. Kim, 3D numerical simulation of seamless pipe piercing process by fluid-structure interaction method, MATEC Web Conf 203 (2018), https://doi.org/10.1051/matecconf/201820306016.
[6] Y. Chastel, A. Diop, S. Fanini, P.O. Bouchard, K. Mocellin, Finite element modeling of tube piercing and creation of a crack, Int. J. Material Form. 1 (SUPPL. 1) (2008) 355–358, https://doi.org/10.1007/s12289-008-0068-2.
[7] Z. Pater, Ł. Wójcik, P. Walczuk, Comparative analysis of tube piercing processes in the two-roll and three-roll mills, Adv. Sci. Technol. Res. J. 13 (1) (2019) 37–45, https://doi.org/10.12913/22998624/102766.
[8] Z. Pater, J. Kazanecki, J. Bartnicki, Three dimensional thermo-mechanical simulation of the tube forming process in Diescher's mill, J. Mater. Process. Technol. 177 (1) (2006) 167–170, https://doi.org/10.1016/j.jmatprotec.2006.03.205.
[9] A. Topa, B.C. Cerik, D.K. Kim, A useful manufacturing guide for rotary piercing seamless pipe by ALE method, J. Mar. Sci. Eng. 8 (10) (Sep. 2020) 756, https://doi.org/10.3390/jmse8100756.
[10] M. Joun, J. Lee, J. Cho, S. Jeong, H. Moon, Quantitative study on mannesmann effect in roll piercing of hollow shaft, Procedia Eng. 81 (2014) 197–202, https://doi.org/10.1016/j.proeng.2014.09.150.
[11] L. Lu, Z. Wang, F. Wang, G. Zhu, X. Zhang, Simulation of tube forming process in mannesmann mill, J. Shanghai Jiao Tong Univ. (Sci.) 16 (3) (2011) 281–285, https://doi.org/10.1007/s12204-011-1144-1.
[12] S. Fanini, A. Ghiotti, S. Bruschi, Evaluation of fracture initiation in the mannesmann piercing process, AIP Conf. Proc. 907 (1) (Apr. 2007) 709–714, https://doi.org/10.1063/1.2729596.
[13] S. Fanini, A. Ghiotti, S. Bruschi, Prediction of the fracture due to mannesmann effect in tube piercing, AIP Conf. Proc. 908 (1) (May 2007) 1407–1412, https://doi.org/10.1063/1.2741006.
[14] A. Ghiotti, S. Fanini, S. Bruschi, P.F. Bariani, Modelling of the mannesmann effect, CIRP Ann. - Manuf. Technol. 58 (1) (2009) 255–258, https://doi.org/10.1016/j.cirp.2009.03.099.
[15] Z. Zhang, et al., Numerical and experimental investigations on Mannesmann effect of nickel-based superalloy, Arch. Civ. Mech. Eng. 22 (3) (2022) 133, https://doi.org/10.1007/s43452-022-00452-2.
[16] A. Murillo-Marrodán, et al., Microstructural and mechanical analysis of seamless pipes made of superaustenitic stainless steel using cross-roll piercing and elongation, Journal of Manufacturing and Materials Processing 7 (2023), https://doi.org/10.3390/jmmp7050185.
[17] H.A. Derazkola, E. Garcia, A. Murillo-Marrodán, Effects of skew rolling piercing process friction coefficient on tube twisting, strain rate and forming velocity, J. Mater. Res. Technol. 25 (2023) 7254–7272, https://doi.org/10.1016/j.jmrt.2023.07.167.
[18] I.N. Yadav, K.B. Thapa, Anisotropic theoretical fatigue damage model for concrete material based on tensile strain Increment-A new novel proposed theory, Results Eng 11 (2021), 100249, https://doi.org/10.1016/j.rineng.2021.100249.
[19] S. Atatreh, M.S. Alyammahi, H. Vasilyan, T. Alkindi, R.A. Susantyoko, Evaluation of the infill design on the tensile properties of metal parts produced by fused filament fabrication, Results Eng 17 (2023), 100954, https://doi.org/10.1016/j.rineng.2023.100954.
[20] H. Aghajani Derazkola, E. Garcia, A. Murillo-Marrodán, Effects of tool-workpiece friction condition on energy consumption during piercing phase of seamless tube production, Key Eng. Mater. 926 (2022) 602–611, https://doi.org/10.4028/p-70x28i.
[21] H. Aghajani Derazkola, E. Garcia, A. Murillo-Marrodán, Effects of tool–workpiece interfaces friction coefficient on power and energy consumption during the piercing phase of seamless tube production, J. Mater. Res. Technol. 19 (2022) 3172–3188, https://doi.org/10.1016/j.jmrt.2022.06.071.
[22] H.A. Derazkola, E. Garcia, A. Murillo-Marrodán, J. Hardell, The effect of temperature and strain rate on the mechanical properties and microstructure of super Cr13 martensitic stainless steel, J. Mater. Res. Technol. 24 (2023) 3464–3476, https://doi.org/10.1016/j.jmrt.2023.04.012.
[23] Z. Zhang, D. Liu, J. Wang, Compression-shear fracture of nickel-based superalloy during rotary tube piercing, Eng. Fract. Mech. (2023), 109777, https://doi.org/10.1016/j.engfracmech.2023.109777.
[24] X.P. Ma, L.J. Wang, C.M. Liu, S.V. Subramanian, Microstructure and properties of 13Cr5Ni1Mo0.025Nb0.09V0.06N super martensitic stainless steel, Mater. Sci. Eng. 539 (2012) 271–279, https://doi.org/10.1016/j.msea.2012.01.093.
[25] Y. Liu, D. Ye, Q. Yong, J. Su, K. Zhao, W. Jiang, Effect of heat treatment on microstructure and property of Cr13 super martensitic stainless steel, J. Iron Steel Res. Int. 18 (11) (2011) 60–66, https://doi.org/10.1016/S1006-706X(11)60118-0.
[26] S. Krizsma, A. Suplicz, Monitoring and modelling the deformation of an aluminium prototype mould insert under different injection moulding and clamping conditions, Results Eng 20 (2023), 101556, https://doi.org/10.1016/j.rineng.2023.101556.
[27] T. Bulzak, Z. Pater, J. Tomczak, Modified hybrid damage criterion for the cross wedge rolling process, J. Manuf. Process. 107 (–505) (2023) 496, https://doi.org/10.1016/j.jmapro.2023.10.075.
[28] Y. V Gamin, S.P. Galkin, A.N. Koshmin, A. Mahmoud Alhaj Ali, X.D. Nguyen, I. S. Eldeeb, High-reduction radial shear rolling of aluminum alloy bars using custom-calibrated rolls, Int. J. Material Form. 17 (1) (2023) 5, https://doi.org/10.1007/s12289-023-01801-z.
[29] H.A. Derazkola, E.G. Gil, A. Murillo-Marrodán, D. Méresse, Review on dynamic recrystallization of martensitic stainless steels during hot deformation: Part i—experimental study, Metals 11 (2021), https://doi.org/10.3390/met11040572.
[30] R. Langbauer, G. Nunner, T. Zmek, J. Klarner, R. Prieler, C. Hochenauer, Modelling of thermal shrinkage of seamless steel pipes using artificial neural networks (ANN) focussing on the influence of the ANN architecture, Results Eng 17 (2023), 100999, https://doi.org/10.1016/j.rineng.2023.100999.
[31] H. Aghajani Derazkola, E. Garcia, A. Murillo-Marrodán, A. Conde Fernandez, Review on modeling and simulation of dynamic recrystallization of martensitic stainless steels during bulk hot deformation, J. Mater. Res. Technol. 18 (2022) 2993–3025, https://doi.org/10.1016/j.jmrt.2022.03.179.